Weierstraß-Institut
für Angewandte Analysis und Stochastik

Leibniz-Institut im Forschungsverbund Berlin e. V.

Preprint ISSN 2198-5855

Volume exclusion effects in perovskite charge transport modeling

Dilara Abdel[1], Nicola E. Courtier[2], Patricio Farrell[1]

submitted: October 28, 2022

[1] Weierstrass Institute
Mohrenstr. 39
10117 Berlin
Germany
E-Mail: dilara.abdel@wias-berlin.de
patricio.farrell@wias-berlin.de

[2] University of Oxford, Engineering Science
Parks Road
Oxford OX1 3PJ
United Kingdom
E-Mail: nicola.courtier@eng.ox.ac.uk

No. 2965
Berlin 2022

2020 *Mathematics Subject Classification.* 35Q81, 35K57.

Key words and phrases. Perovskite modeling, drift-diffusion equations, volume exclusion effects, current density.

This work was partially supported by the Leibniz competition.

Edited by
Weierstraß-Institut für Angewandte Analysis und Stochastik (WIAS)
Leibniz-Institut im Forschungsverbund Berlin e. V.
Mohrenstraße 39
10117 Berlin
Germany

Fax: +49 30 20372-303
E-Mail: preprint@wias-berlin.de
World Wide Web: http://www.wias-berlin.de/

Volume exclusion effects in perovskite charge transport modeling

Dilara Abdel, Nicola E. Courtier, Patricio Farrell

Abstract

Due to their flexible material properties, perovskite materials are a promising candidate for many semiconductor devices such as lasers, memristors, LEDs and solar cells. For example, perovskite-based solar cells have recently become one of the fastest growing photovoltaic technologies. Unfortunately, perovskite devices are far from commercialization due to challenges such as fast degradation. Mathematical models can be used as tools to explain the behavior of such devices, for example drift-diffusion equations portray the ionic and electric motion in perovskites. In this work, we take volume exclusion effects on ion migration within a perovskite crystal lattice into account. This results in the formulation of two different ionic current densities for such a drift-diffusion model – treating either the mobility or the diffusivity as density-dependent while the other quantity remains constant. The influence of incorporating each current density description into a model for a typical perovskite solar cell configuration is investigated numerically, through simulations performed using two different open source tools.

1 Introduction

Arguably, only few materials have gained such interest within photovoltaics as perovskites [1]. These materials show promise for use in applications including lasers, memristors, LEDs and solar cells. Recently, perovskite-silicon tandem cells have become more efficient than high performing single junction silicon solar cells [2]. However, for the commercialization of perovskite based solar cells a couple of challenges need to be overcome, especially the fast degradation of such devices. Further, there does not exist profound knowledge about the exact physical operation mechanisms within such devices. Thus, adequate models and simulation tools are needed to better understand the device physics.

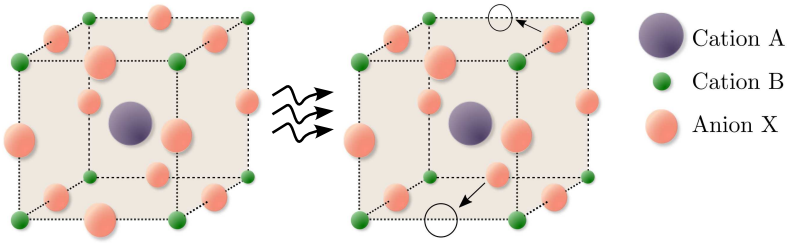

Figure 1: A perovskite unit cell under idealized conditions (left) and with realistic crystal defects (right).

Perovskites form a class of crystalline solids of the form ABX_3 with two cations A, B and an anion X which are not fixed to the crystalline lattice. To be more precise, crystal defects occur that dynamically appear and reappear. They leave void spaces, called vacancies, within the crystal which can be occupied by the migrating ions, visualized in the right unit cell in Figure 1. This continually changing crystalline structure affects the electric charge carriers and cannot be neglected. In perovskites, the movement of numerous negatively charged anions has a strong influence on the transport of charge. The inclusion of ion migration can be investigated using different model approaches, for example by atomistic Density Functional Theory (DFT) calculations [3, 4], equivalent circuit models [5, 6] or charge transport modeling with drift-diffusion equations resulting in a system of partial differential equations.

DOI 10.20347/WIAS.PREPRINT.2965

The latter approach is the most convenient one concerning the computational cost while still maintaining a direct connection of the output to the device physics. Initial charge transport models incorporating ionic movement for perovskite solar cells (PSCs) such as [7–9] were formulated, but ignored the finite size of ions, meaning the presented models did not bound the density of available lattice within a perovskite crystal. Later, models were introduced tackling this issue advocating for a nonlinear diffusion current density for ionic charge carriers [10, 11] or for linear diffusion but a modified drift current density [12]. To the best of our knowledge, the two approaches were not compared yet and their influence on a perovskite charge transport model was not assessed. The remainder of this paper is organized as follows: in Section 2 the model describing charge transport in perovskites will be introduced and discussed. Afterwards, in Section 3 volume exclusion effects and their thermodynamically consistent inclusion into the model will be presented. This results in two different formulations of the ionic current density: treating either the mobility or the diffusivity as density-dependent while the other quantity remains constant. Then, in Section 4 the influence of both current density descriptions on a PSC configuration will be numerically discussed. Finally, we conclude in Section 5.

2 Model Equations

Let the domain $\overline{\mathbf{\Omega}} \subset \mathbb{R}^d$, $d \in \{1, 2, 3\}$, correspond to a perovskite material, which usually forms a subdomain of a full device architecture and let α denote a moving charge carrier (electrons n, holes p or anion vacancies a). Further, we define the corresponding density as n_α and ψ as the electric potential. Then, the carriers' movement can be described by [10, 13]

$$-\nabla \cdot (\varepsilon_s \nabla \psi(\mathbf{x}, t)) = \sum_{\alpha \in \{n,p,a\}} z_\alpha q \left(n_\alpha(\mathbf{x}, t) - C_\alpha(\mathbf{x}) \right), \mathbf{x} \in \mathbf{\Omega},\ t \geq 0, \tag{1a}$$

$$z_\alpha q \partial_t n_\alpha(\mathbf{x}, t) + \nabla \cdot \mathbf{j}_\alpha(\mathbf{x}, t) = z_\alpha q r_\alpha(\mathbf{x}, t), \qquad \mathbf{x} \in \mathbf{\Omega},\ t \geq 0. \tag{1b}$$

Here, ε_s denotes the dielectric permittivity given as the product of the relative material permittivity and the vacuum dielectric constant, q denotes the elementary charge and z_α the charge number which is for electrons and holes $z_n = -1, z_p = 1$ and for anion vacancies $z_a = 1$. Further, the donor and acceptor doping is given by C_n, C_p whereas the mean vacancy concentration is given by C_a. A reaction/generation mechanism can be described by a rate r_α. For example, the sum total of bulk recombination mechanisms R and an external photo-generation G can be applied to both electrons and holes, i.e. $r_n = r_p = G(\mathbf{x}) - R(n_n(\mathbf{x}, t), n_p(\mathbf{x}, t))$. For the anion vacancies, we may assume $r_a = 0$. Finally, the motion of charge carriers is described by the current density $\mathbf{j}_\alpha$. Note that the set of unknowns can be given either in terms of the electric potential ψ and the densities of moving carriers n_α, $\alpha = n, p, a$, or in terms of $(\psi, \varphi_n, \varphi_p, \varphi_a)$, where φ_α denotes the respective quasi Fermi potentials. These potentials are linked to the charge carrier densities via the state equation

$$n_\alpha = N_\alpha \mathcal{F}_\alpha\Big(\eta_\alpha(\psi, \varphi_\alpha)\Big),\ \eta_\alpha = z_\alpha \frac{q(\varphi_\alpha - \psi) + E_\alpha}{k_B T}, \quad \alpha = n, p, a, \tag{2}$$

where N_n, N_p are the effective conduction and valence band density of states and E_n, E_p the conduction and valence band-edge energies. Further, N_a is the maximum ion vacancy concentration and E_a the formation energy. The parameter k_B refers to the Boltzmann constant and T to the temperature. We call the function $\mathcal{F}_\alpha$, which relates the carrier densities to the respective quasi Fermi potentials, the statistics function. For non-degenerate semiconductors the statistics function for electric charge carriers is an exponential, but in general, in the degenerate case, it is given by an integral equation,

corresponding to the Fermi-Dirac integral of order $1/2$ (inorganic semiconductor) or the Gauss-Fermi integral (organic semiconductor). For electrons and holes, the perovskite model (1) is supplemented with the following current density descriptions

$$\mathbf{j}_n = -qz_n\Big(D_n\nabla n_n + z_n\mu_n n_n\nabla\psi\Big),\ \mathbf{j}_p = -qz_p\Big(D_p\nabla n_p + z_p\mu_p n_p\nabla\psi\Big), \tag{3}$$

where the diffusion coefficients D_n, D_p and the mobilities μ_n, μ_p, are related via the generalized Einstein relation [10]

$$D_\alpha = \mu_\alpha U_T g_\alpha\left(\frac{n_\alpha}{N_\alpha}\right),\quad g_\alpha\left(\frac{n_\alpha}{N_\alpha}\right) = \frac{n_\alpha}{N_\alpha}(\mathcal{F}_\alpha^{-1})'\left(\frac{n_\alpha}{N_\alpha}\right),\quad \alpha = n, p, \tag{4}$$

where U_T is the thermal voltage and g_α the diffusion enhancement. When modeling non-degenerate semiconductors we have $g_n = g_p = 1$ with constant mobilities and diffusion coefficients, but in general it holds that $g_n, g_p \geq 1$. Finally, to discuss physically meaningful current density descriptions for anion vacancies, volume exclusion effects need to be discussed. Note that, the model is supplemented with homogeneous (no-flux) Neumann boundary conditions for the anion vacancies as well as suitable initial and boundary conditions for all species.

3 Volume exclusion effects

In the fields of electrolytes and battery modeling, the need to take the finite size of ions into account is already established [14–16]. To be consistent with non-equilibrium thermodynamics the finite density of available lattice sites within a perovskite crystal needs to be reflected by the charge transport model. It is common to refer to this phenomenon as *volume exclusion effects*, *excluded-volume effects*, *steric effects* or *limiting ion depletion*. Within our framework, this can be incorporated implicitly by limiting the vacancy density saturation. Figure 2 visualizes the density of ions and of ion vacancies within the

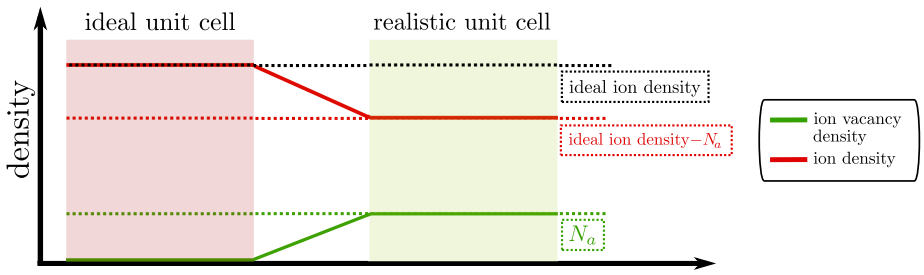

Figure 2: Development of the ion density (red) and the ion vacancy density (red) within two different perovskite crystal unit cell configurations.

two possible perovskite unit cell configurations illustrated in Figure 1. The red area corresponds to an idealized unit cell with no vacancies (green curve) and an ion density (red curve) equal to the ideal ion density of the unit cell. Contrarily, the green area shows the densities for a unit cell with defects. Bounding in this case the vacancy density from above, implies the existence of a lower bound for the ion density. To include this effect in a thermodynamically consistent manner, we use a statistical relation as in (2) for the anion vacancies given by the Fermi-Dirac integral of order -1

$$n_a = N_a\mathcal{F}_a\Big(\eta_a(\psi,\varphi_a)\Big) = \frac{N_a}{\exp(-\eta_a)+1},\quad \eta_a = \frac{q(\varphi_a-\psi)+E_a}{k_BT}. \tag{5}$$

Note that φ_a is frequently called the electrochemical potential, but to be consistent with semiconductor theory, we refer to it as a quasi Fermi potential. Now, possible descriptions for the ion vacancy current density $\mathbf{j}_a$ can be discussed. We start from this formulation

$$\mathbf{j}_a = -q\mu_a z_a^2 n_a \nabla\varphi_a,$$

showing the proportionality of the charge carrier current density to its thermodynamic driving force – the negative gradient of the quasi Fermi potential. For diffusion on a lattice, the generalized Einstein relation between the diffusion coefficient and mobility of the anion vacancies likewise holds [15]

$$D_a = \mu_a U_T g_a\left(\frac{n_a}{N_a}\right), \quad g_a\left(\frac{n_a}{N_a}\right) = \frac{1}{1-\frac{n_a}{N_a}}, \tag{6}$$

where g_a is sometimes called the activity coefficient instead of diffusion enhancement. Whether we assume now a constant mobility or a constant diffusivity results in two different drift-diffusion current density descriptions.

Nonlinear diffusion. On the one hand, to be consistent with the electron and hole flux descriptions we can assume a constant mobility $\mu_a = \overline{\mu}_a$, apply the generalized Einstein relation (6) and make use of the state equation (5) such that the current density comprises nonlinear diffusion [10]

$$\mathbf{j}_{a,\text{diff}} = -qz_a\overline{\mu}_a U_T\left(g_a\left(\frac{n_a}{N_a}\right)\nabla n_a + \frac{z_a}{U_T}n_a\nabla\psi\right). \tag{7}$$

Modified drift. On the other hand, a constant diffusion coefficient $D_a = \overline{D}_a$, called the chemical diffusivity, allows us to express the mobility in terms of the activity coefficient g_a. This leads to a current density expression with linear diffusion but with a modified drift term [12, 15]

$$\mathbf{j}_{a,\text{drift}} = -qz_a\overline{D}_a\left(\nabla n_a + \frac{z_a}{U_T g_a\left(\frac{n_a}{N_a}\right)}n_a\nabla\psi\right). \tag{8}$$

Note that both current densities, (7) and (8), lead to two *different* charge transport models which have the *same* steady state solution due to the homogeneous Neumann boundary condition. To the best of our knowledge, there does not exist a work where the influence of both current density descriptions on the charge transport model behavior for perovskites was compared and investigated. Thus, in the following we look closer at the numerical performances of the two current densities introduced in (7) and (8).

4 Numerical simulation of a PSC device

In this section, we simulate a three-layer PSC device, where the perovskite is sandwiched between two doped non-perovskite semiconductor transport layers. To be more precise, MAPI is used as the perovskite material, while PCBM is chosen for the electron and PEDOT:PSS for the hole transport layer. A schematic of the device architecture is shown in Figure 3. Note that anion vacancies move solely within the perovskite (red area), whereas electrons, holes and the electric potential are defined across the whole device.

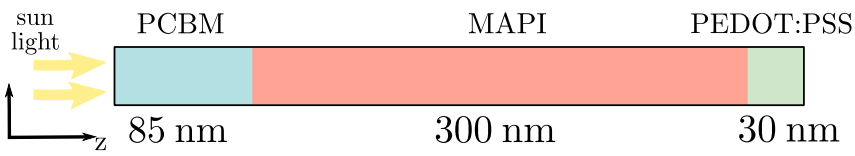

Figure 3: Schematic diagram of the simulated device configuration with ohmic contacts. The electron transport layer (blue) is given by PCBM, whereas for the hole transport layer (red) PEDOT:PSS is used.

Designing the benchmark. Let us introduce the dimensionless scaling factor

$$\epsilon = \frac{C_a}{N_a} = \frac{\text{average anion vacancy density}}{\text{maximum anion vacancy density}},$$

where C_a is incorporated into the model via the right-hand side of the Poisson equation (1a) and N_a is a model parameter in the state equation (5). If ϵ tends to zero, then we neglect the finite size of ions, resulting in a Boltzmann relation between n_a and φ_a (meaning $\mathcal{F}_a \approx \exp$). Contrarily, if $\epsilon = 1$, then ionic movement is suppressed and, thus, the model reduces to the classical van Roosbroeck system. The precise choice of ϵ is strongly dependent on the perovskite material and may be calculated by DFT calculations as performed by [17]. Given sufficient relaxation time, a charge transport model of the form (1) on a domain as depicted in Figure 3 based on either (7) or (8) results in the same steady state solution. Thus, of special interest is the simulation of current-voltage (J-V) scan protocols, where the model is far from an equilibrium state. For this, we simulate a linear J-V scan protocol with a scan rate of 40mV$/$s for an applied bias between 0V and 1.2V. This implies that the scan ends at $t = 30$s. Note, that during the scan the outer boundary conditions for the ohmic contacts vary with time and the steady state is not reached. The simulations were performed in one dimension and the chosen parameters can be found in Table 1. We choose $\overline{\mu}_a = 1 \times 10^{-10}\text{cm}^2/(\text{Vs})$ and $\overline{D}_a = 2.59 \times 10^{-12}\text{cm}^2/\text{s}$.

Physical quantity	symbol	value			unit
		PCBM	perovskite	PEDOT:PSS	
Layer thickness		8.5×10^{-6}	3.0×10^{-5}	3.0×10^{-6}	cm
Relative permittivity		3	23	4	
Conduction band-edge energy	E_n	-3.8	-3.8	-3.0	eV
Valence band-edge energy	E_p	-6.2	-5.4	-5.1	eV
Eff. conduction band DoS	N_n	1×10^{19}	1×10^{19}	1×10^{20}	cm^{-3}
Eff. valence band DoS	N_p	1×10^{19}	1×10^{19}	1×10^{20}	cm^{-3}
Mean anion vacancy density	C_a	–	1.0×10^{18}	–	cm^{-3}
Doping density	C_n	2.09×10^{18}	0.0	0.0	cm^{-3}
Doping density	C_p	0.0	0.0	2.09×10^{18}	cm^{-3}
Electron mobility	μ_n	1×10^{-3}	20	0.1	$\text{cm}^2/(\text{Vs})$
Hole mobility	μ_p	1×10^{-3}	20	0.1	$\text{cm}^2/(\text{Vs})$
Radiative recombination coeff.		0.0	3.6×10^{-12}	0.0	cm^3/s
SRH lifetimes (electrons & holes)		1.0×10^{100}	1.0×10^{-7}	1.0×10^{100}	s
SRH trap energy		-5.0	-4.6	-4.05	eV

Table 1: Parameter values at a temperature $T = 300$K from [11]. SRH denotes Shockley-Read-Hall recombination.

To simulate the PSC device, we make use of two open source tools `Ionmonger` [8, 13] and `ChargeTransport.jl` [18, 19]. While `ChargeTransport.jl` uses a finite volume method for the spatial discretization implemented in Julia, `Ionmonger` is based on a finite element method written in Matlab. The same non-uniform grid spacing as introduced by [13] is used, whereas a uniform time mesh is utilized in `ChargeTransport.jl` and an adaptive one in `IonMonger`. To primarily focus on the impact of the different current density descriptions, other effects such as photogeneration and surface recombination are neglected in the simulations.

Electric potential and vacancy density profiles. Figure 4 shows the evolution of the electric potential within the perovskite layer (area shaded in red). Additionally, the evolution of the vacancy density in the vicinity of each perovskite/transport layer interface is depicted in Figure 5. Both profiles are visualized for a model based on the nonlinear diffusion current density (7) and a model based on the modified drift current (8) for two choices of ϵ reflecting low and high volume exclusion. The colored lines correspond to a solution calculated with `ChargeTransport.jl` whereas the black dotted lines indicate respective solutions calculated with `Ionmonger`. Brighter colors indicate later time. First, note that both software tools based on different discretization techniques yield near-identical results. Hence, we can compare the impact of the different current density descriptions independent of the numerical method.

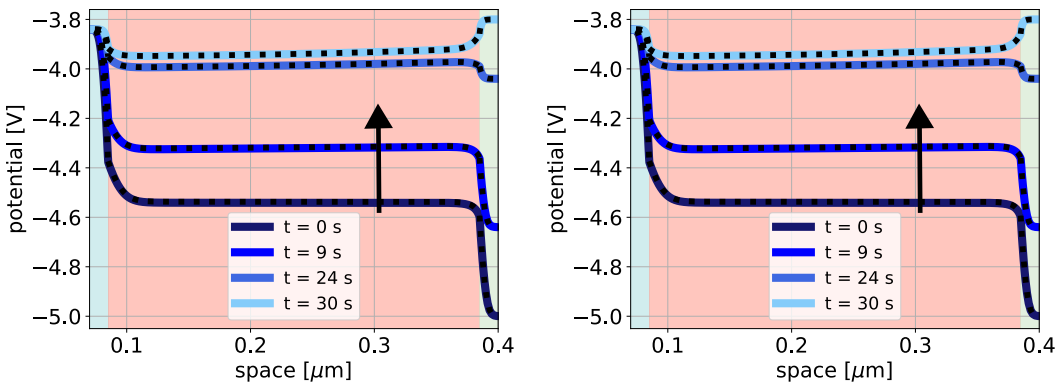

nonlinear diffusion, $\epsilon = 0.01$ modified drift, $\epsilon = 0.01$

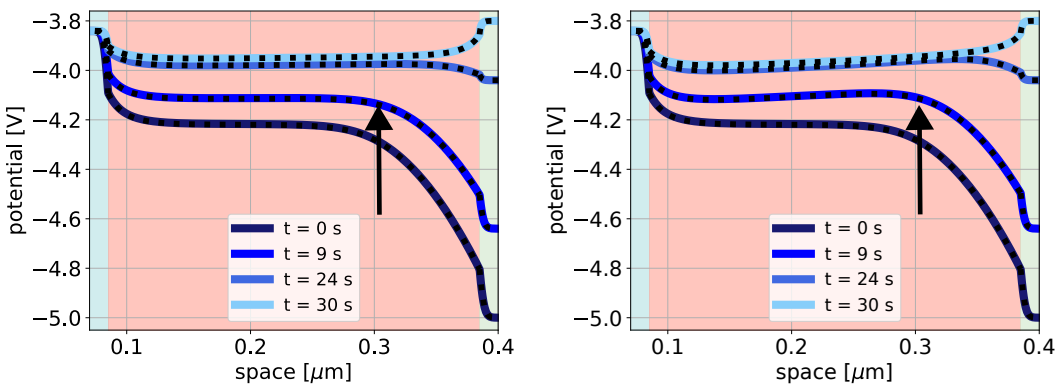

nonlinear diffusion, $\epsilon = 0.9$ modified drift, $\epsilon = 0.9$

Figure 4: Evolution of the electric potential ψ in the perovskite layer solving the model (1) based on the nonlinear diffusion current density (7) (first column) and for the model based on the modified drift current (8) (second column). The first row shows the case of $\epsilon = 0.01$ (low exclusion, $E_a = -4.66$eV) and the second row of $\epsilon = 0.9$ (high exclusion, $E_a = -4.16$eV). The arrows indicate the direction of increasing time.

Not surprisingly, for $\epsilon = 0.01$ no difference in the electrostatic potential evolution (Figure 4, first row) and in the vacancy density profiles (Figure 5, top set of four) can be observed. Contrarily for high volume exclusion, i.e. larger ϵ, the modified drift current density (8) causes a slower decrease of the ion density at the right perovskite interface (Figure 5, second set of rows).

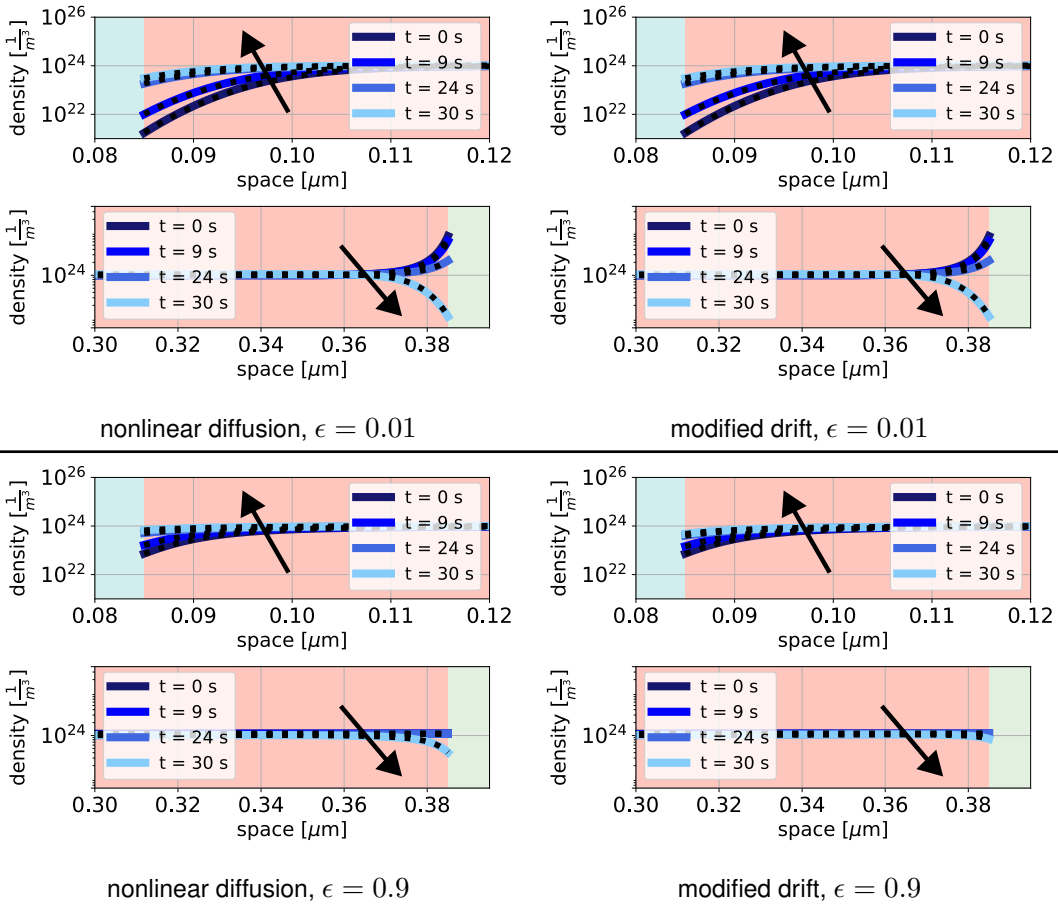

Figure 5: Evolution of the vacancy density n_a at the left and right perovskite/transport layer interface for the model based on the nonlinear diffusion current (7) (first column) and for a model based on the modified drift current (8) (second column). The first set of rows shows the case of $\epsilon = 0.01$ ($E_a = -4.66$eV) and the second set of rows (below the line) corresponds to $\epsilon = 0.9$ ($E_a = -4.16$eV). The arrows indicate the direction of increasing time. No differences can be observed in the case of low exclusion, whereas a slower evolution of the ion profile can be observed in the case of high exclusion and a modified drift current density.

This can be seen from the electric potential gradients remaining larger for the modified drift approach for larger times such as $t = 24$ s and $t = 30$ s in Figure 4 (second row). Furthermore, Figure 6 shows that the difference in the calculated electric potentials, i.e. $\psi_{\text{drift}} - \psi_{\text{diff}}$, is approximately two orders of magnitude larger for high volume exclusion. Even though the difference in the electric potentials (Figure 6) behaves similarly for all depicted times t, Figure 7 indicates in the case of high excluded-volume effects the difference in the vacancy density at the end time $t = 30$s is comparably large. This trend can be likewise observed for different choices of ϵ in Figure 8, where the L^∞ error between the calculated electric potentials and the vacancy densities with respect to ϵ are depicted. Both L^∞ errors are increasing with higher effects of excluded-volume for all visualized times $t > 0$. It seems that the difference in the vacancy densities becomes most visible for larger times and larger ϵ (Figure 8, right)

and increases the most for the end time $t = 30$s. Note that the end time here does not refer to a steady state, but to the end time of the scan protocol. Thus, we can conclude that in the case of high volume exclusion the time scales of converging towards a steady state for a model based on either nonlinear diffusion or on a modified drift current density are diverging.

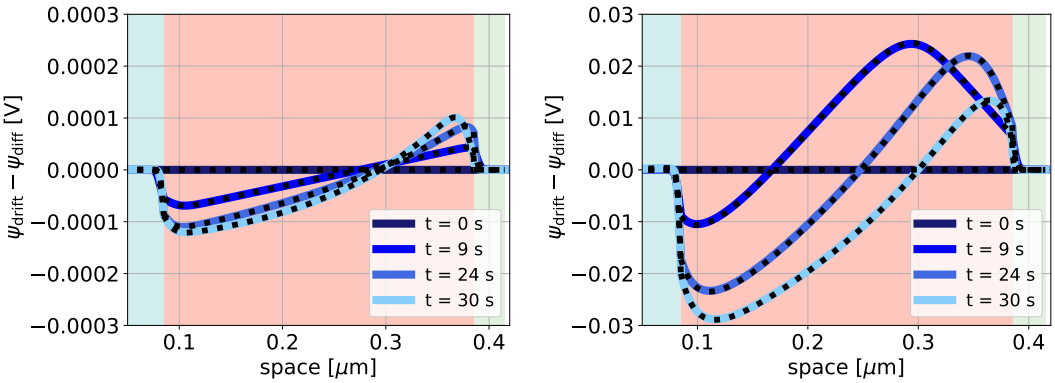

Figure 6: Difference between calculated electrostatic potentials depicted in Figure 4 based on either a modified drift or a nonlinear diffusion approach, i.e. the error $\psi_{\text{drift}} - \psi_{\text{diff}}$ is shown for $\epsilon = 0.01$ (left) and $\epsilon = 0.9$ (right). The scale of the y-axes differs by two orders of magnitudes.

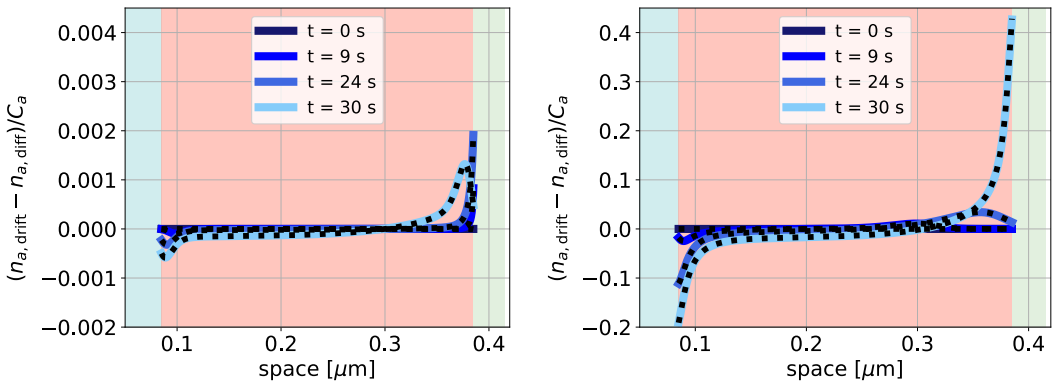

Figure 7: Difference between calculated vacancy densities depicted in Figure 5 based on either a modified drift or a nonlinear diffusion approach scaled by the average vacancy density for $\epsilon = 0.01$ (left) and $\epsilon = 0.9$ (right). The scale of the y-axes differs by two orders of magnitudes.

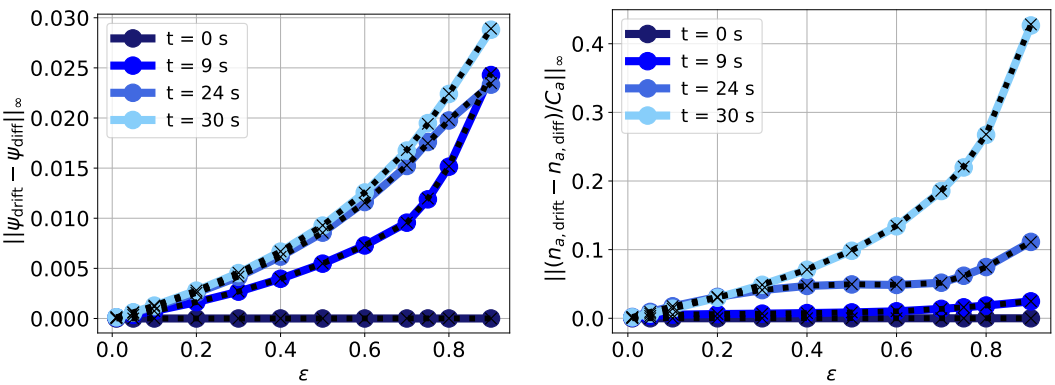

Figure 8: L^∞ error between the electric potentials (left) and the vacancy densities (right) from a model based on either a nonlinear diffusion or a modified drift current density for variations of ϵ.

Current-voltage curves. Lastly, the influence of the different current density descriptions on J-V curves (simulated in the dark) is investigated in Figure 9 and Figure 10. Again, colored curves correspond to solutions calculated with `ChargeTransport.jl`, while black dotted lines are the solutions received when using `IonMonger`. Brighter colors indicate higher volume exclusion which is reflected in the choice of ϵ. First, both approaches reveal in Figure 9 that the larger the choice for ϵ, the more the respective J-V curve is shifted to the left, i.e. the higher the recombination rate. Second, when employing the modified drift approach a greater change in the J-V curves with respect to the difference between the smallest and largest ϵ can be noticed (see Figure 9). Third, for the model based on the modified drift current density, the impact of volume exclusion becomes observable in the J-V curves at a smaller value of ϵ.

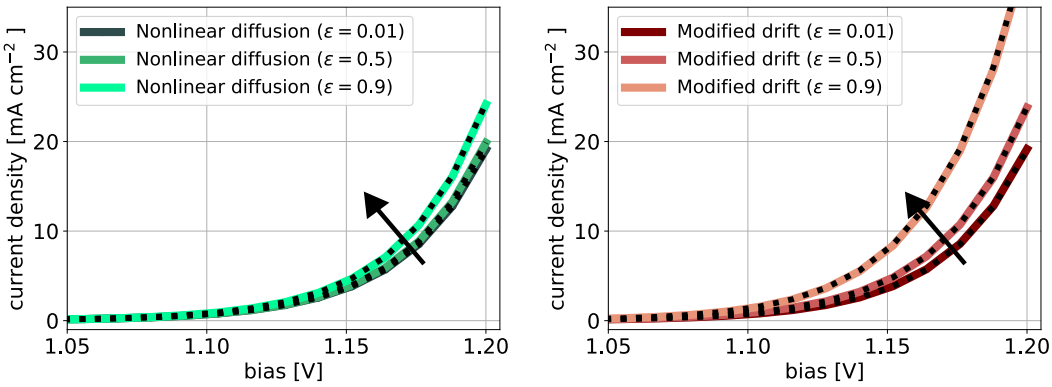

Figure 9: Current-voltage curves for nonlinear diffusion (left) and modified drift (right) for variations of ϵ. The arrows indicate the direction of increasing ϵ. For larger values of ϵ the diode opens earlier.

The trends in the recombination current can be explained, as in [20], in terms of the distribution of the electric potential across the cell. In this model, the dominant form of recombination is hole-limited bulk SRH recombination. At earlier times ($t = 0$ and $t = 9$s in Figure 4), large positive electric fields keep holes and electrons apart. However, at later times ($t = 24$ and $t = 30$s), we observe that the electric field at the perovskite/HTL interface decreases for increasing ϵ.

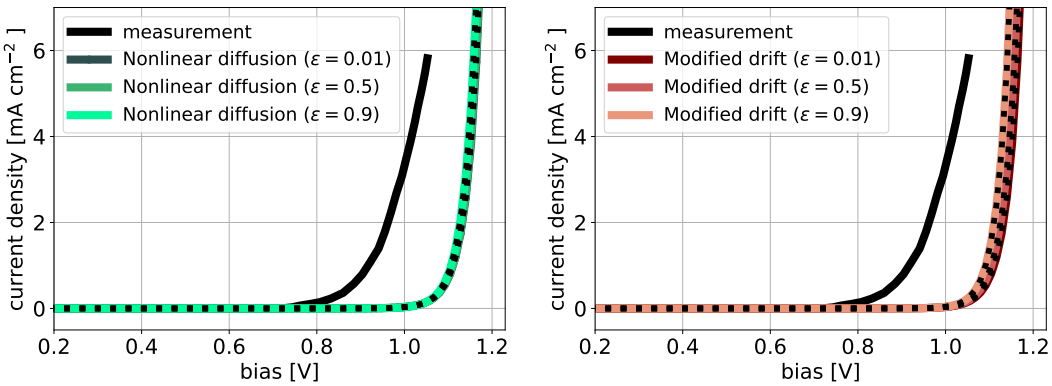

Figure 10: Simulated current-voltage curves for nonlinear diffusion (left) and modified drift (right) for variations of ϵ in comparison with measurement curves from [7].

Smaller positive fields/larger negative fields allow a greater number of holes from the transport layer to enter the perovskite, leading to increased recombination and higher currents, as shown in Figure

9. For the modified drift current density, at large ϵ, a negative electric field also emerges across the bulk of the perovskite due to the slower migration of ions (see Figure 5, second set of rows), which further enhances the rate of recombination. In Figure 10, the simulated J-V curves are compared to the measured curves from [7] for the same device set-up as illustrated in Figure 3. Now, one may argue that the difference between either nonlinear diffusion or modified drift current density may be minor. But, for the sake of simplicity, other effects such as surface mechanisms were entirely neglected in this study. Additional physical effects may exhibit different behavior depending on whether a charge transport model is based on nonlinear diffusion or modified drift current densities. Thus, it is important to develop the capabilities to investigate the underlying ion migration mechanism in order to formulate accurate device models.

5 Summary and Outlook

For a perovskite charge transport model we discussed how to properly include volume exclusion effects via the statistics function in the case of migrating ionic charge carriers. This study provides in two possible current density descriptions: nonlinear diffusion (7) and a modified drift (8). Both descriptions recover special cases of the charge transport model in the limit of ignoring the finite size of ions or suppressing ionic movement. Further, the models based on both current density descriptions converge towards the same steady solution. In numerical simulations, the influence of both descriptions on the internal states and on the current-voltage behavior of a three-layer PSC configuration was investigated. The simulations were performed with two different open source tools based on different numerical methods of solution, yielding near-identical results. In the case of high exclusion, the modified drift current leads to a slower evolution of the ion profile. This reveals a greater influence of volume exclusion effects on model predictions based on a modified drift current density description. Studying the impact of these approaches for a generalized charge transport model including further physically meaningful mechanisms is of interest in the future. Also, studying the impact on the performance of alternative device architectures based on other perovskite and transport layer materials can be a topic of future research. Finally, the parameter sensitivity of other physical quantities such as band-edge energies or the dielectric permittivity was neglected even though they have an impact on the electric potential and thus on the vacancy density behavior. This could also be investigated in a continuation of this work.

References

[1] N. Tessler and Y. Vaynzof, “Insights from device modeling of perovskite solar cells,” *ACS Energy Letters*, vol. 5, pp. 1260–1270, 04 2020.

[2] National Renewable Energy Laboratory (NREL), “Best research-cell efficiency chart.” `https://www.nrel.gov/pv/cell-efficiency.html` (accessed 2022-09-30), Jan. 2022.

[3] C. Eames, J. M. Frost, P. R. F. Barnes, B. C. O’Regan, A. Walsh, and M. S. Islam, “Ionic transport in hybrid lead iodide perovskite solar cells,” *Nature Communications*, vol. 6, p. 7497, Nov 2015.

[4] S. Tan, I. Yavuz, N. De Marco, T. Huang, S.-J. Lee, C. S. Choi, M. Wang, S. Nuryyeva, R. Wang, Y. Zhao, H.-C. Wang, T.-H. Han, B. Dunn, Y. Huang, J.-W. Lee, and Y. Yang, “Steric impediment of ion migration contributes to improved operational stability of perovskite solar cells,” *Advanced Materials*, vol. 32, no. 11, p. 1906995, 2020.

[5] E. C. Smith, C. L. C. Ellis, H. Javaid, L. A. Renna, Y. Liu, T. P. Russell, M. Bag, and D. Venkataraman, "Interplay between ion transport, applied bias, and degradation under illumination in hybrid perovskite p-i-n devices," *The Journal of Physical Chemistry C*, vol. 122, no. 25, pp. 13986–13994, 2018.

[6] D. Moia, I. Gelmetti, P. Calado, W. Fisher, M. Stringer, O. Game, Y. Hu, P. Docampo, D. Lidzey, E. Palomares, J. Nelson, and P. R. F. Barnes, "Ionic-to-electronic current amplification in hybrid perovskite solar cells: ionically gated transistor-interface circuit model explains hysteresis and impedance of mixed conducting devices," *Energy Environ. Sci.*, vol. 12, pp. 1296–1308, 2019.

[7] P. Calado, A. Telford, D. Bryant, X. Li, J. Nelson, B. O'Regan, and P. Barnes, "Evidence for ion migration in hybrid perovskite solar cells with minimal hysteresis," *Nature Communications*, vol. 7, 2016.

[8] N. E. Courtier, G. Richardson, and J. M. Foster, "A fast and robust numerical scheme for solving models of charge carrier transport and ion vacancy motion in perovskite solar cells," *Applied Mathematical Modelling*, 2018.

[9] M. T. Neukom, A. Schiller, S. Züfle, E. Knapp, J. Ávila, D. Pérez-del Rey, C. Dreessen, K. P. Zanoni, M. Sessolo, H. J. Bolink, and B. Ruhstaller, "Consistent device simulation model describing perovskite solar cells in steady-state, transient, and frequency domain," *ACS Applied Materials & Interfaces*, vol. 11, no. 26, pp. 23320–23328, 2019.

[10] D. Abdel, P. Vágner, J. Fuhrmann, and P. Farrell, "Modelling charge transport in perovskite solar cells: Potential-based and limiting ion depletion," *Electrochimica Acta*, vol. 390, p. 138696, 2021.

[11] P. Calado, I. Gelmetti, B. Hilton, M. Azzouzi, J. Nelson, and P. Barnes, "Driftfusion: an open source code for simulating ordered semiconductor devices with mixed ionic-electronic conducting materials in one dimension," *Journal of Computational Electronics*, vol. 21, pp. 1–32, 08 2022.

[12] N. E. Courtier, *Modelling ion migration and charge carrier transport in planar perovskite solar cells*. PhD thesis, University of Southampton, 2019.

[13] N. E. Courtier, J. M. Cave, A. B. Walker, G. Richardson, and J. M. Foster, "Ionmonger: a free and fast planar perovskite solar cell simulator with coupled ion vacancy and charge carrier dynamics," *Journal of Computational Electronics*, vol. 18, pp. 1435–1449, 2019.

[14] I. Borukhov, D. Andelman, and H. Orland, "Adsorption of large ions from an electrolyte solution: a modified poisson–boltzmann equation," *Electrochimica Acta*, vol. 46, no. 2, pp. 221 – 229, 2000.

[15] M. Z. Bazant, "Theory of chemical kinetics and charge transfer based on nonequilibrium thermodynamics," *Accounts of Chemical Research*, vol. 46, no. 5, pp. 1144–1160, 2013. PMID: 23520980.

[16] V. Sulzer, S. J. Chapman, C. P. Please, D. A. Howey, and C. W. Monroe, "Faster lead-acid battery simulations from porous-electrode theory: Part I. physical model," *Journal of The Electrochemical Society*, vol. 166, no. 12, pp. A2363–A2371, 2019.

[17] A. Walsh, D. O. Scanlon, S. Chen, X. G. Gong, and S.-H. Wei, "Self-regulation mechanism for charged point defects in hybrid halide perovskites," *Angewandte Chemie International Edition*, vol. 54, no. 6, pp. 1791–1794, 2015.

[18] D. Abdel, P. Farrell, and J. Fuhrmann, "Assessing the quality of the excess chemical potential flux scheme for degenerate semiconductor device simulation," *Optical and Quantum Electronics*, vol. 53, no. 163, 2021.

[19] D. Abdel, P. Farrell, and J. Fuhrmann, "ChargeTransport.jl: Simulating charge transport in semiconductors." `https://github.com/PatricioFarrell/ChargeTransport.jl`, 2022.

[20] N. E. Courtier, "Interpreting ideality factors for planar perovskite solar cells: Ectypal diode theory for steady-state operation," *Physical Review Applied*, vol. 14, p. 024031, aug 2020.